Confined Crystallization of Polyethylene Oxide in Nanolayer Assemblies

Haopeng Wang, *et al.*

Science **323**, 757 (2009);
DOI: 10.1126/science.1164601

Science (print ISSN 0036-8075; online ISSN 1095-9203) is published weekly, except the last week in December, by the American Association for the Advancement of Science, 1200 New York Avenue NW, Washington, DC 20005.

References and Notes

1. C. Weidner, P. Kroupa, *Mon. Not. R. Astron. Soc.* **348**, 187 (2004).
2. D. F. Figer, *Nature* **434**, 192 (2005).
3. F. D. Kahn, *Astron. Astrophys.* **37**, 149 (1974).
4. M. G. Wolfire, J. P. Cassinelli, *Astrophys. J.* **319**, 850 (1987).
5. T. Nakano, T. Hasegawa, C. Norman, *Astrophys. J.* **450**, 183 (1995).
6. J. Jijina, F. C. Adams, *Astrophys. J.* **462**, 874 (1996).
7. H. W. Yorke, C. Sonnhalter, *Astrophys. J.* **569**, 846 (2002).
8. M. M. Marinak *et al.*, *Phys. Rev. Lett.* **75**, 3677 (1995).
9. F. H. Shu, S. Tremaine, F. C. Adams, S. P. Ruden, *Astrophys. J.* **358**, 495 (1990).
10. M. R. Krumholz, R. I. Klein, C. F. McKee, *Astrophys. J.* **656**, 959 (2007).
11. K. M. Kratter, C. D. Matzner, M. R. Krumholz, *Astrophys. J.* **681**, 375 (2008).
12. B. D. Mason *et al.*, *Astron. J.* **115**, 821 (1998).
13. H. Sana, E. Gosset, Y. Nazé, G. Rauw, N. Linder, *Mon. Not. R. Astron. Soc.* **386**, 447 (2008).
14. C. F. McKee, J. C. Tan, *Nature* **416**, 59 (2002).
15. C. F. McKee, J. C. Tan, *Astrophys. J.* **585**, 850 (2003).
16. H. Beuther *et al.*, *Astron. Astrophys.* **466**, 1065 (2007).
17. A. A. Goodman, P. J. Benson, G. A. Fuller, P. C. Myers, *Astrophys. J.* **406**, 528 (1993).
18. R. I. Klein, *J. Comput. Appl. Math.* **109**, 123 (1999).
19. M. R. Krumholz, C. F. McKee, R. I. Klein, *Astrophys. J.* **611**, 399 (2004).
20. R. T. Fisher, thesis, University of California, Berkeley (2002).
21. M. R. Krumholz, R. I. Klein, C. F. McKee, J. Bolstad, *Astrophys. J.* **667**, 626 (2007).
22. A. I. Shestakov, S. S. R. Offner, *J. Comput. Phys.* **227**, 2154 (2008).
23. See supporting material on *Science* Online.
24. G. Lodato, W. K. M. Rice, *Mon. Not. R. Astron. Soc.* **358**, 1489 (2005).
25. M. R. Bate, *Mon. Not. R. Astron. Soc.* **314**, 33 (2000).
26. H. W. Yorke, P. Bodenheimer, *Astrophys. J.* **525**, 330 (1999).
27. C. D. Matzner, C. F. McKee, *Astrophys. J.* **545**, 364 (2000).
28. J. Alves, M. Lombardi, C. J. Lada, *Astron. Astrophys.* **462**, L17 (2007).
29. M. R. Krumholz, C. F. McKee, R. I. Klein, *Astrophys. J.* **618**, L33 (2005).
30. N. J. Turner, E. Quataert, H. W. Yorke, *Astrophys. J.* **662**, 1052 (2007).

31. Supported by NSF grants AST-0807739 (M.R.K.) and AST-0606831 (R.I.K. and C.F.M.); the Spitzer Space Telescope Theoretical Research Program, provided by NASA through a contract issued by the Jet Propulsion Laboratory (M.R.K.); NASA through Astrophysics Theory and Fundamental Physics Program grants NAG 05-12042 and NNG 06-GH96G (R.I.K. and C.F.M.); and the U.S. Department of Energy at Lawrence Livermore National Laboratory under contract B-542762 (R.I.K., S.S.R.O., and A.J.C.). This research used the Datastar system at the NSF San Diego Supercomputer Center (grant UCB267).

Supporting Online Material

www.sciencemag.org/cgi/content/full/1165857/DC1
SOM Text
Figs. S1 to S5
Movie S1
References

12 September 2008; accepted 11 December 2008
Published online 15 January 2009;
10.1126/science.1165857
Include this information when citing this paper.

Confined Crystallization of Polyethylene Oxide in Nanolayer Assemblies

Haopeng Wang,[1] Jong K. Keum,[1] Anne Hiltner,[1]* Eric Baer,[1] Benny Freeman,[2] Artur Rozanski,[3] Andrzej Galeski[3]

The design and fabrication of ultrathin polymer layers are of increasing importance because of the rapid development of nanoscience and nanotechnology. Confined, two-dimensional crystallization of polymers presents challenges and opportunities due to the long-chain, covalently bonded nature of the macromolecule. Using an innovative layer-multiplying coextrusion process to obtain assemblies with thousands of polymer nanolayers, we discovered a morphology that emerges as confined polyethylene oxide (PEO) layers are made progressively thinner. When the thickness is confined to 20 nanometers, the PEO crystallizes as single, high-aspect-ratio lamellae that resemble single crystals. Unexpectedly, the crystallization habit imparts two orders of magnitude reduction in the gas permeability.

Crystalline polymers, such as polyethylene, polypropylene, poly(ethylene terephthalate), and nylon, have been broadly used as gas-barrier films in food, medicine, and electronics packaging, benefiting thereby from their low cost, easy processing, and mechanical toughness. Good barrier properties are imparted by the ability of polymer chains to crystallize into semicrystalline materials with both crystalline and amorphous phases (*1*). The efficiency of chain packing is such that the crystalline phase is generally regarded as impermeable to even small gas molecules, and gas transport is seen as occurring through the amorphous regions (*2*). The processing conditions can be readily varied to control the amount of crystallinity and chain orientation and to tune the barrier properties of the final product (*3*). With the growing use of polymers as thin and ultrathin films (*4*, *5*), morphologies have been found resulting from constrained two-dimensional (2D) polymer crystallization (*4*, *6*). These crystalline morphologies could possess gas permeability characteristics that are not expected from the bulk polymers.

Despite confinement, crystallization of polymer chains follows the conventional habit whereby polymer chains fold back and forth into stems to form crystalline lamellae with a thickness of ~10 to 20 nm. It is typical of crystallization from the isotropic melt that the lamellae are organized in a spherulitic morphology (*7*). However, the processes of nucleation and growth that control the crystallization kinetics can be profoundly affected by nanoscale confinement. The thickness of ultrathin polymer layers, usually a few tens of nanometers, is comparable to or a small multiple of the lamellar crystal thickness. Hence, the isotropic growth of lamellar crystals is greatly hampered, and crystallization under confinement can produce a specific lamellar crystal orientation. Often, the preferred lamellar crystal orientation is vertical to the layer (edge-on) (*8*, *9*, *10*). However, at the other extreme, lamellar crystal orientation parallel to the layer (flat-on) is observed (*6*, *11*–*14*). Although the mechanisms for the specific lamellar orientation during confined crystallization are still under investigation (*15*, *16*), it is believed that the confined crystals will show anisotropic properties.

The 2D crystallization of polymers is conventionally studied with thin films or block copolymers that contain a crystallizable block. In the former, crystallizable layers with nanometer to submicron thicknesses are prepared by a solution process such as spin-coating (*4*, *17*) or Langmuir-Blodgett (*18*) techniques. This approach is limited by the solvent requirement and by the small amount of material that can be fabricated. In the latter, a layered morphology on the nanometer scale is achieved as a consequence of microphase separation of the dissimilar blocks. If the crystallization temperature of the crystallizable block is below the order-disorder transition temperature (*19*), crystallization occurs with confinement in the layer-normal direction. A wide range of crystallizable blocks have been studied (*8*, *11*–*14*, *16*). However, elucidation of the structure-property relationships has been hindered by the need to synthesize the block copolymers and by the shear alignment that is required to construct the uniformly oriented phase structure (*20*).

In contrast to the self-assembled confinement created with microphase-separated block copolymers (*21*), layer-multiplying coextrusion uses forced assembly to create films with hundreds or thousands of alternating layers of two polymers (*22*, *23*). Almost any melt-processable polymer can be fabricated into kilometers of nanolayered films, and layers less than 10 nm in thickness have been made. Although the amount of material in a single layer is very small, the properties of the confined layer are multiplied many-fold by the number of identical layers in the assembly. This enables us to use conventional methods to probe size-scale-dependent properties. Polyethylene oxide (PEO) was coextruded with poly

[1]Department of Macromolecular Science and Engineering, Case Western Reserve University, Cleveland, OH 44106–7202, USA. [2]Department of Chemical Engineering, University of Texas at Austin, Austin, TX 78758, USA. [3]Centre of Molecular and Macromolecular Studies, Polish Academy of Sciences, 90-363 Lodz, Poland.

*To whom correspondence should be addressed. E-mail: ahiltner@case.edu

(ethylene-*co*-acrylic acid) (EAA), a copolymer with much lower crystallinity than PEO (fig. S1). Films with 33, 257, and 1025 alternating EAA and PEO layers were coextruded with various thicknesses and various composition ratios, including (EAA/PEO vol/vol) 50/50, 70/30, 80/20 and 90/10 (table S1). The nominal PEO layer thickness, which was calculated from the number of layers, the composition ratio, and the film thickness, varied from 3.6 μm to 8 nm. Nonlayered control films were also extruded.

Permeability to small molecules is an important performance property of polymer films. Gas transport also provides a probe into the solid-state structure (*3*). The oxygen permeability (*P*) was first measured on films where the PEO and EAA layers had the same thickness. The layer thickness was varied by changing the number of coextruded layers and the overall film thickness while maintaining the composition at 50/50. The results, plotted in Fig. 1A as a function of layer thickness, unexpectedly showed a steady decrease in the oxygen permeability as the EAA and PEO layers became thinner. A comparable reduction was found for carbon dioxide permeability.

The series model for layered assemblies gives the gas permeability as

$$P_{\parallel} = \left(\frac{\phi_{PEO}}{P_{PEO}} + \frac{1-\phi_{PEO}}{P_{EAA}}\right)^{-1} \quad (1)$$

where ϕ_{PEO} is the volume fraction of PEO, and P_{PEO} and P_{EAA} are the permeabilities of PEO and EAA control films, respectively. Using the determined values of 0.38 barrer (*24*) and 2.30 barrer for P_{PEO} and P_{EAA}, Eq. 1 gave the oxygen permeability of an EAA/PEO 50/50 layered assembly as 0.65 barrer. Only the film with the thickest layers conformed to this prediction.

Noting that PEO is substantially less permeable to oxygen than EAA, Eq. 1 predicts that $P_{//}$ will be quite sensitive to P_{PEO} even if ϕ_{PEO} is relatively small. To ascertain whether a dramatic change in the PEO permeability was responsible for the layer thickness effect, numerous films that varied in both the composition ratio and the layer thickness were tested. Although the measured values of *P* scattered, depending on the composition ratio, when an effective PEO permeability was extracted,

$$P_{PEO,eff} = \phi_{PEO}\left(\frac{1}{P} - \frac{1-\phi_{PEO}}{P_{EAA}}\right)^{-1} \quad (2)$$

the data collapsed to a single curve when $P_{PEO,eff}$ was plotted as a function of the PEO layer thickness (Fig. 1B). Only the results for the thicker PEO microlayers conformed to Eq. 2, with $P_{PEO,eff} \approx P_{PEO}$, as indicated by the dashed line. Deviation below the line was seen with 1-μm-thick PEO layers. The lowest $P_{PEO,eff}$ was achieved with 20-nm layers, and the value of 0.0052 barrer was almost 2 orders of magnitude less than P_{PEO}.

It seemed likely that crystallization in a confined space resulted in an unusual crystalline morphology that endowed the PEO nanolayers with exquisitely low permeability. However, differential scanning calorimetry revealed that even in the thinnest layers, both PEO and EAA possessed the same melting enthalpy and the same melting

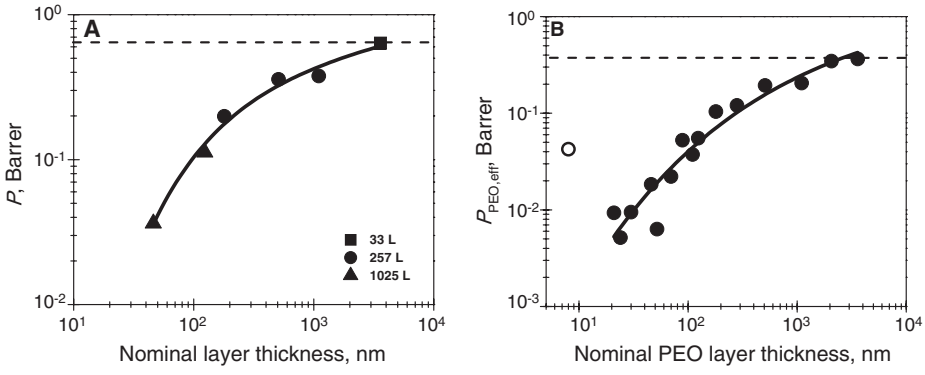

Fig. 1. The effect of layer thickness on oxygen permeability. (**A**) Oxygen permeability of films with equal volume fractions of EAA and PEO. The dashed line indicates $P_{//}$ calculated from Eq. 1. (**B**) Oxygen permeability of the PEO layers from films of varying composition calculated from Eq. 2. The dashed line indicates P_{PEO}. The open symbol is for a film with PEO layer breakup. The solid lines are drawn to guide the eyes.

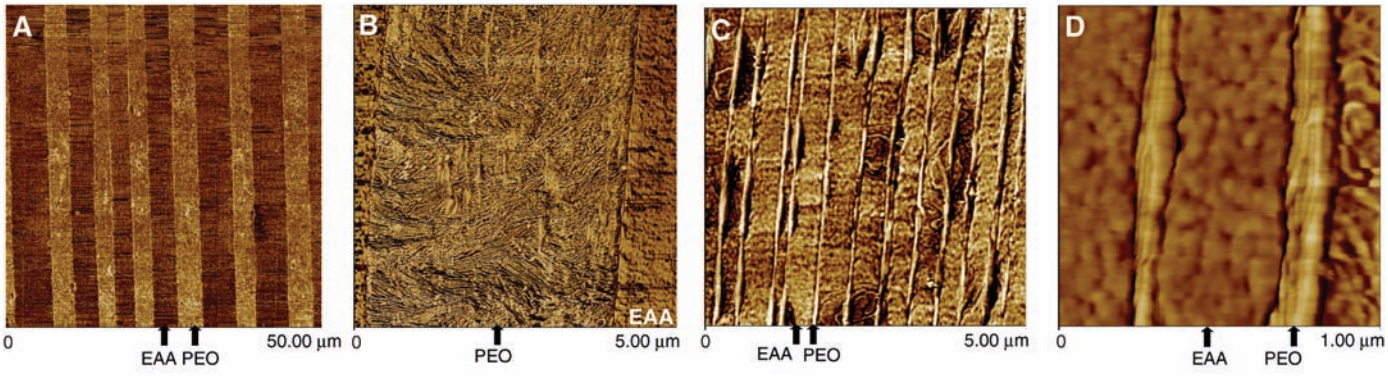

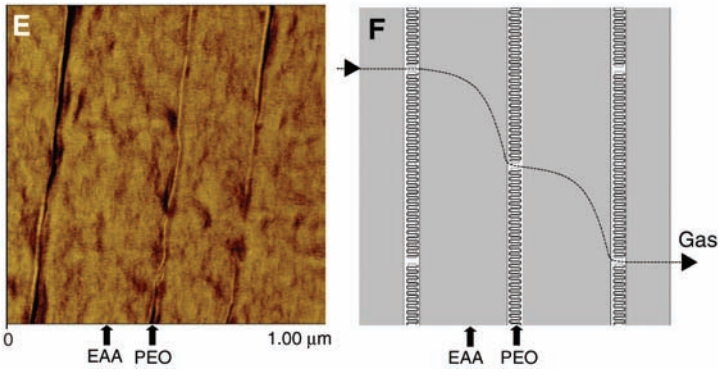

Fig. 2. AFM phase images of partial cross sections of the layered EAA/PEO films. The PEO layer has substantially higher crystallinity than the EAA layers and hence appears bright in the AFM images. (**A**) A low-resolution image of an EEA/PEO film with 50/50 composition, 33 alternating layers, and nominal PEO layer thickness of 3.6 μm. (**B**) A higher-resolution image showing the spherulitic morphology of the 3.6-μm-thick PEO layer. (**C**) A low-resolution image of an EAA/PEO film with 70/30 composition, 1025 alternating layers and nominal PEO layer thickness of 110 nm. (**D**) A higher-resolution image of the 110-nm-thick PEO layers showing the oriented stacks of PEO lamellae. (**E**) A high-resolution image of an EAA/PEO film with 90/10 composition, 1025 alternating layers, and nominal PEO layer thickness of 20 nm showing that the PEO layers crystallized as single, extremely large lamellae. (**F**) A schematic showing the gas diffusion pathway through the layered assembly with 20-nm-thick PEO layers. The arrows identify the EAA layers and PEO layers.

temperature as the control films, which were 153 J/g and 66°C for PEO, and 98 J/g and 98°C for EAA, respectively (fig. S2 and table S2). Thus, any unusual crystalline morphology that provided the very low permeability of PEO nanolayers was not accompanied by changes in the crystallinity or in the lamellar thickness.

The layers were viewed by microtoming the film through the thickness and examining the exposed surface in atomic force microscope (AFM). A region from the cross section of a film with 3.6-μm-thick PEO layers confirmed the layer continuity (Fig. 2A). Although there was some nonuniformity, the average layer thickness was close to the calculated nominal layer thickness. A higher magnification image showed the sharp boundaries between EAA and PEO layers (Fig. 2B). The spherulitic morphology of the bright PEO layer closely resembled that of PEO crystallized from the unconfined melt. It was expected that the properties of the PEO layers would also be the same and, indeed, the oxygen permeability of films with thick PEO layers closely conformed to Eq. 2 with $P_{PEO,eff} \approx P_{PEO}$.

Another pair of images in Fig. 2, C and D, compares a film with 110-nm-thick PEO layers. The images confirmed the continuity of the thin PEO layers and the close correspondence between the average layer thickness and the nominal thickness. At higher magnification, the effect of confinement on crystallization of the PEO layer shows that PEO crystallized as stacks of three to five long, thin lamellae oriented in the plane of the layer. When the PEO layer thickness was reduced to 20 nm, most of the PEO layers crystallized as single, extremely large lamellae whose lateral dimensions frequently exceeded the field of the AFM image (Fig. 2E). Coincidence between the layer thickness, which was determined by the extrusion conditions, and the thickness of PEO lamellae, about 20 nm, facilitated crystallization of the layers as single lamellae. The single lamellae could be thought of as very large single crystals (*25*). If the layer thickness was reduced to 8 nm, the layers broke up, which caused the increased permeability of the film with 8-nm PEO layers.

The lamellar crystalline core is considered impermeable, and the lamellar fold surfaces constitute the permeable amorphous regions. For a single layer of flat-on lamellae, as in the PEO nanolayer, the diffusion pathway depends on the frequency of defects such as lamellar edges (Fig. 2F). Structurally, the nanolayered assembly resembles a dispersion of impermeable platelets of given aspect ratio. If the platelets are oriented perpendicular to the flux, the permeability of the composite is expressed as (*26*)

$$P = P_{EAA}\left[1 + \frac{\alpha^2\phi^2}{4(1-\phi)}\right]^{-1} \quad (3)$$

where ϕ is the volume fraction of impermeable platelets and α is the aspect ratio of the platelets defined as length divided by width. In this case, ϕ was taken as the volume fraction of the PEO crystalline phase. For the thinnest PEO nanolayers, the aspect ratio from Eq. 3 was as high as 120, which meant a lateral dimension of more than 2 μm for lamellae 20 nm thick. Gradually increasing the PEO layer thickness relaxed the restriction on 3D growth, which allowed crystallization of lamellar stacks and permitted randomization of the lamellar orientation. Also, the increased area density of nuclei in individual layers reduced the lateral dimension of lamellae. The gradual change in crystallization habit from single lamellae to isotropic spherulites paralleled a gradual increase in the permeability of the PEO layer.

Confirmation of the oriented lamellar morphology and details of the global orientation were obtained with small-angle x-ray scattering (SAXS) and wide-angle x-ray scattering (WAXS). The SAXS examined the periodic arrangement of lamellar crystals within the constituent layers. By aligning the incident x-ray beam parallel to the normal direction (ND), the extrusion direction (ED), and the transverse direction (TD), the orientation of lamella was determined (fig. S3). The scattering patterns indicated that the long spacing of the PEO and EAA lamellae in layered films were 22.0 ± 0.6 nm and 10.8 ± 0.5 nm, respectively, nearly the same as in the control films. Isotropic scattering patterns in all three directions from 3.6 μm PEO layers indicated that the PEO layers were too thick for PEO lamellae to feel any substantial confinement effect. However, as the PEO layer thickness decreased to 110 nm, highly oriented meridional two-point scattering features appeared in the ED and TD patterns, which indicated that stacked PEO lamellae were oriented primarily parallel to the layer surface due to the confinement. The extremely weak first-order peak from 20 nm PEO layers indicated that they existed predominantly as single lamellae rather than as stacks (fig. S4).

The orientation of the PEO chains in the crystal was examined with 2D WAXS and pole

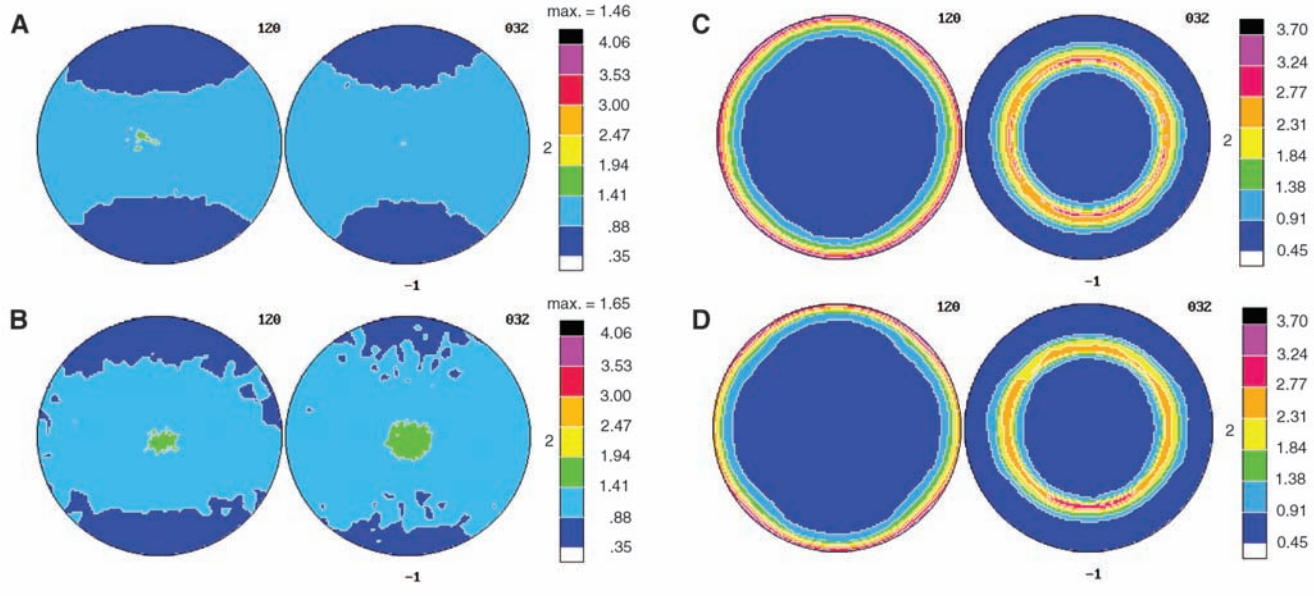

Fig. 3. Pole figures of normals to the (120) and (032) planes of the PEO monoclinic crystals (*27*). The extrusion direction is vertical and the transverse direction is horizontal. The normal direction is in the center of the pole figure. (**A**) The PEO control film. (**B**) An EAA/PEO film with 50/50 composition, 33 alternating layers, and nominal PEO layer thickness of 3.6 μm. (**C**) An EAA/PEO film with 70/30 composition, 1025 alternating layers, and nominal PEO layer thickness of 110 nm. Orientation of the (120) planes is perpendicular to the layer plane, and orientation of the (032) planes is at 67°. (**D**) An EAA/PEO film with 90/10 composition, 1025 alternating layers, and nominal PEO layer thickness of 20 nm.

figures. Consistent results were obtained by these two techniques. From the pole figures of normals to the (120) and (032) planes of PEO (*27*), it is seen that there is no preferred orientation of crystals in the control film except for a slight orientation due to the extrusion process (Fig. 3A). In Fig. 3B, the film with 3.6-μm-thick PEO layers also showed only very weak orientation. In contrast, the film with 110-nm-thick PEO layers showed a very strong orientation of the (120) and also the (032) planes (Fig. 3C). Nearly all the (120) planes that contained polymer chains were perpendicular to the film plane. This meant that the fold surfaces of the lamellar PEO crystals were in the plane of the layer. Upon decreasing the PEO layer thickness to 20 nm, the preferred orientation of PEO lamellae parallel to the layers seemed even stronger, as indicated by the narrower ring at the pole figure circumference (Fig. 3D). The (120) planes were distributed evenly in the plane of film, always being perpendicular to the film surface. The pole figures for (032) normal in Fig. 3, C and D, resembled rings exactly offset by 67°, as predicted by the crystallographic unit cell for the preferred orientation of PEO lamellae parallel to the layer interface (*16*). Again, the ring for the (032) normal in Fig. 3D was much narrower than in Fig. 3C.

The crystal orientation of PEO in confined nanolayers essentially reproduced the crystal structure of PEO blocks in self-assembled PS-*b*-PEO diblock copolymers (*14*, *16*). Comparing the sharpness of the WAXS pattern, considerably higher orientation was achieved by physically confining a high-molecular-weight PEO between force-assembled layers than by confining a low-molecular-weight PEO block between self-assembled lamellae with covalent links. When the thickness confinement occurred on the size scale of the usual lamellar thickness, the PEO layers crystallized as single lamellae with extremely large aspect ratios. It was suggested that the lamellae could be thought of as large, impermeable single crystals.

The coextrusion process, which operates with readily available polymers, now makes it possible to fabricate nanolayered polymeric structures in sufficient quantities to probe the structure-property relationships of the morphologies resulting from nanoscale confinement. For design and execution of packaging strategies, polymer nanolayers can be incorporated into conventional polymeric films with the right barrier properties for less cost, which in turn may reduce the environmental and energy impact.

References and Notes

1. D. C. Bassett, *Principles of Polymer Morphology* (Cambridge Univ. Press, Cambridge, 1981).
2. D. H. Weinkauf, D. R. Paul, in *Barrier Polymers and Structures*, W. J. Koros, Ed. (American Chemical Society, Washington, DC 1990), pp. 60–91.
3. A. Hiltner, R. Y. F. Liu, Y. S. Hu, E. Baer, *J. Polym. Sci. Pt. B Polym. Phys.* **43**, 1047 (2005).
4. C. W. Frank *et al.*, *Science* **273**, 912 (1996).
5. S. Goffri *et al.*, *Nat. Mater.* **5**, 950 (2006).
6. G. Reiter *et al.*, *Lect. Notes Phys.* **714**, 179 (2007).
7. E. Baer, A. Hiltner, H. D. Keith, *Science* **235**, 1015 (1987).
8. I. W. Hamley *et al.*, *Macromolecules* **29**, 8835 (1996).
9. T. E. Bernal-Lara, R. Y. F. Liu, A. Hiltner, E. Baer, *Polymer (Guildf.)* **46**, 3043 (2005).
10. Y. Jin *et al.*, *J. Polym. Sci. Pt. B Polym. Phys.* **42**, 3380 (2004).
11. R. M. Ho *et al.*, *Macromolecules* **37**, 5985 (2004).
12. Y. S. Sun *et al.*, *Macromolecules* **39**, 5782 (2006).
13. U. Mukai, R. E. Cohen, A. Bellare, R. J. Albalak, *J. Appl. Polym. Sci.* **70**, 1985 (1998).
14. M.-S. Hsiao *et al.*, *Macromolecules* **41**, 8114 (2008).
15. Y. Ma, W. Hu, G. Reiter, *Macromolecules* **39**, 5159 (2006).
16. L. Zhu *et al.*, *J. Am. Chem. Soc.* **122**, 5957 (2000).
17. S. Napolitano, M. Wübbenhorst, *J. Phys. Condens. Matter* **19**, 205121 (2007).
18. B. Li, A. R. Esker, *Langmuir* **23**, 2546 (2007).
19. F. S. Bates, G. H. Fredrickson, *Annu. Rev. Phys. Chem.* **41**, 525 (1990).
20. Z.-R. Chen, J. A. Kornfield, S. D. Smith, J. T. Grothaus, M. M. Satkowski, *Science* **277**, 1248 (1997).
21. G. M. Whitesides, B. Grzybowski, *Science* **295**, 2418 (2002).
22. R. Y. F. Liu, Y. Jin, A. Hiltner, E. Baer, *Macromol. Rapid Commun.* **24**, 943 (2003).
23. R. Y. F. Liu, T. E. Bernal-Lara, A. Hiltner, E. Baer, *Macromolecules* **37**, 6972 (2004).
24. 1 Barrer = $10^{-10}\frac{cm^3(STP)cm}{cm^2\ s\ cmHg}$, where STP is standard temperature and pressure.
25. P. H. Geil, *Polymer Single Crystals* (Wiley-Interscience, New York, 1963).
26. E. L. Cussler, S. E. Hughes, W. J. Ward III, R. Aris, *J. Membr. Sci.* **38**, 161 (1988).
27. The PEO reflection labeled (032) actually contains overlapped reflections from (032), ($\bar{1}$32), (112), ($\bar{2}$12), ($\bar{1}$24), ($\bar{2}$04), and (004), which have similar *d*-spacing of ~0.39 nm, with that from (032) being the strongest. They cannot be easily separated in (032) pole figure. Details can be found in (*16*).

28. This research was supported by the NSF Center for Layered Polymeric Systems (grant DMR-0423914).

Supporting Online Material

www.sciencemag.org/cgi/content/full/323/5915/757/DC1
Materials and Methods
SOM Text
Figs. S1 to S5
Tables S1 and S2
References

13 August 2008; accepted 26 November 2008
10.1126/science.1164601

Nitrogen-Doped Carbon Nanotube Arrays with High Electrocatalytic Activity for Oxygen Reduction

Kuanping Gong,[1] Feng Du,[1] Zhenhai Xia,[2] Michael Durstock,[3] Liming Dai[1,4]*

The large-scale practical application of fuel cells will be difficult to realize if the expensive platinum-based electrocatalysts for oxygen reduction reactions (ORRs) cannot be replaced by other efficient, low-cost, and stable electrodes. Here, we report that vertically aligned nitrogen-containing carbon nanotubes (VA-NCNTs) can act as a metal-free electrode with a much better electrocatalytic activity, long-term operation stability, and tolerance to crossover effect than platinum for oxygen reduction in alkaline fuel cells. In air-saturated 0.1 molar potassium hydroxide, we observed a steady-state output potential of −80 millivolts and a current density of 4.1 milliamps per square centimeter at −0.22 volts, compared with −85 millivolts and 1.1 milliamps per square centimeter at −0.20 volts for a platinum-carbon electrode. The incorporation of electron-accepting nitrogen atoms in the conjugated nanotube carbon plane appears to impart a relatively high positive charge density on adjacent carbon atoms. This effect, coupled with aligning the NCNTs, provides a four-electron pathway for the ORR on VA-NCNTs with a superb performance.

The oxygen reduction reaction (ORR) at the cathode of fuel cells (*1*) plays a key role in controlling the performance of a fuel cell, and efficient ORR electrocatalysts are essential for practical applications of the fuel cells (*2*, *3*). The ORR can proceed either through (i) a four-electron process to combine oxygen with electrons and protons directly, when coupled with oxidation on the anode, to produce water as the end product, or (ii) a less efficient two-step, two-electron pathway involving the formation of hydrogen peroxide ions as an intermediate (*2*, *3*). Alkaline fuel cells with platinum-loaded carbon as an electrocatalyst for the four-electron ORR were developed for the Apollo lunar mission in the 1960s (*4*), but their large-scale commercial application has been precluded by the high cost of the requisite noble metals. Apart from its high cost, the Pt-based electrode also suffers from its susceptibility to time-dependent drift (*5*) and CO deactivation (*6*).

Recent intensive research efforts in reducing or replacing Pt-based electrode in fuel cells have led to the development of new ORR electrocatalysts, including Pt-based alloys (*7*), transition metal chalcogenides (*8*), carbon nanotube–supported metal particles (*9*–*11*), enzymatic electrocatalytic systems (*12*), and even conducting poly(3,4-

[1]Departments of Chemical and Materials Engineering, University of Dayton, 300 College Park, Dayton, OH 45469, USA. [2]Department of Mechanical Engineering, University of Akron, Akron, OH 44325, USA. [3]Materials and Manufacturing Directorate, Air Force Research Laboratory, RXBP, Wright-Patterson Air Force Base, OH 45433, USA. [4]Department of Chemistry and University of Dayton Research Institute and Institute for the Development and Commercialization of Advanced Sensor Technology and Wright Brothers Institute, Dayton, OH 45469, USA.

*To whom correspondence should be addressed. E-mail: ldai@udayton.edu

Supporting Online Material for

Confined Crystallization of Polyethylene Oxide in Nanolayer Assemblies

Haopeng Wang, Jong K. Keum, Anne Hiltner,* Eric Baer,
Benny Freeman, Artur Rozanski, Andrzej Galeski

*To whom correspondence should be addressed. E-mail: ahiltner@case.edu

Published 6 February 2009, *Science* **323**, 757 (2009)
DOI: 10.1126/science.1164601

This PDF file includes:

Supporting Online Material for

Confined Crystallization of Polyethylene Oxide in Nanolayer Assemblies

Haopeng Wang,[1] Jong K. Keum,[1] Anne Hiltner,[1] Eric Baer,[1] Benny Freeman,[2] Artur Rozanski,[3] Andrzej Galeski[3]*

[1]Department of Macromolecular Science and Engineering, Case Western Reserve University, Cleveland, OH 44106-7202

[2]Department of Chemical Engineering, University of Texas at Austin, Austin, TX 78758

[3]Centre of Molecular and Macromolecular Studies, Polish Academy of Sciences, 90-363 Lodz, Poland

*Corresponding author: Anne Hiltner (E-mail: ahiltner@case.edu)

Content of SOM

Materials

Poly(ethylene oxide) (PEO) with molecular weight of 200 kg/mol (PolyOx WSR N80) and ethylene acrylic acid copolymer (EAA) with 9.7 wt% acrylic acid (Primacor1410) were obtained from The Dow Chemical Company. Both EAA and PEO were dried under vacuum before processing.

Methods

Films with alternating layers of PEO and EAA with EAA outer layers were fabricated using the layer multiplication process (S*1*, S*2*). The schematic drawing of layer-multiplying coextrusion in **Figure S1** shows how a series of n multiplying elements combines two dissimilar polymers as $2^{(n+1)}+1$ alternating layers. The extruder, multipliers and die temperatures were set to 190 °C to ensure matching viscosities of the two polymer melts. Multilayered films with 33, 257 and 1025 alternating EAA and PEO layers were coextruded as films of various thicknesses and various composition ratios (vol/vol) including (EAA/PEO) 50/50, 70/30, 80/20 and 90/10. The nominal layer thickness was calculated from the number of layers, the composition ratio and the film thickness (**Table S1**). The films were stored at ambient temperature in desiccators to prevent moisture absorption.

Oxygen permeability at 23^{o}C, 0% relative humidity and 1 atm pressure was measured with a MOCON OX-TRAN 2/20. The instrument was calibrated with National Institute of Standards and Technology certified Mylar film of known O_2 transport characteristics. The specimens were carefully conditioned in the instrument, as described previously (S*3*). The O_2 permeability P was calculated from the steady state flux J as

$$P = J\frac{l}{\Delta p} \tag{S1}$$

where l is the film thickness and Δp is the difference of the oxygen partial pressure across the film. For each film, the average P from two specimens is reported.

Differential scanning calorimentry (DSC) was conducted with a Perkin-Elmer DSC-7 at a heating rate 10 °C min^{-1}. The film density was determined by hydrostatic weighing using a balance and a density determination kit (Mettler Toledo Model XS205). Iso-octane (99.8 % pure, Sigma Aldrich) with density of 0.692 g cm^{-3} was used as the auxiliary liquid (S4). The density of the EAA film was 0.936 g cm^{-3} and that of the PEO film was 1.217 g cm^{-3}.

Embedded films were microtomed through the thickness at -75 ºC with a cryo-ultramicrotome (MT6000-XL from RMC) and cross-sections were examined with an atomic force microscope (AFM) in order to visualize the layers and the layer morphology. Phase and height images of the cross-section were recorded simultaneously at ambient temperature in air using the tapping mode of the Nanoscope IIIa MultiMode scanning probe (Digital Instruments).

Small-angle X-ray scattering (SAXS) and wide-angle X-ray scattering (WAXS) patterns were obtained by aligning the incident X-ray beam parallel to the normal direction (ND), the extrusion direction (ED) and the transverse direction (TD) of the film. SAXS measurements were carried out using a rotating anode X-ray generator (Rigaku RU 300, 12 kW) equipped with two laterally graded multilayer optics in a side-by-side arrangement, giving a highly focused parallel beam of monochromatic Cu Kα radiation (λ= 0.154 nm). The monochromatic X-ray beam operated at 50 kV and 100 mA was

collimated using three pinholes and the diameter of X-ray beam at sample position was approximately 700 μm. For the collection of ED and TD SAXS patterns, since the dimensions of the films (42~282 μm thick and 2 mm wide) were smaller than the collimated X-ray beam, the X-ray beam was aligned at an angle of ~3^{o} relative to ED and TD to avoid total reflection. The critical angle for the total reflection is usually on the order of a few tenths of a degree. On the other hand, in order to collect ND SAXS patterns, the X-ray beam was aligned along the direction parallel to the ND. Two dimensional (2D) SAXS patterns were collected by using a 2D gas filled multiwire detector (Rigaku) with a spatial resolution of 1024×1024 pixels. The X-ray exposure times for ED, TD and ND SAXS patterns were 9 hours. The sample-to-detector distance was 1.5 m and the scattering vector q was calibrated using a silver behenate (AgBe) standard, which had (001) peak position at q=1.076 nm^{-1}. A beam stop placed in front of the area detector allowed monitoring of the intensity of the direct beam. Based on the intensity of the direct beam, all SAXS images were corrected for background scattering, dark current and sample absorption.

WAXS measurements were performed using a Statton camera coupled to a Philips PW 1830 X-ray generator (Cu Kα radiation, λ= 0.154 nm) operated at 30 kV and 35 mA. The collimated beam diameter was 250 μm. 2D WAXS images were collected using imaging plate and exposed imaging plates were read with a Fujifilm FDL5000 image plate reader. The sample-to-detector distance was 60 mm and the diffraction angle was calibrated using a CaF_2 standard. Several film pieces were stacked and glued with isocyanate 10s glue. The thickness of the stack was approximately 0.5 mm. The stacks were exposed in the three orthogonal directions. For the ED and TD directions, the film

stack was sectioned perpendicular to the plane of the film to obtain a dimension of 1 mm in the X-ray beam direction.

The orientation of the crystalline phase of PEO was also studied by means of X-ray scattering with pole figures. For an overview of this technique see Ref.(S5) A WAXS system consisting of a computer-controlled pole figure device associated with a wide-angle goniometer coupled to a sealed tube X-ray generator operating at 50 kV and 30mA (Philips) was used in this study. The X-ray beam consisted of Cu Kα radiation filtered electronically and by Ni filter. The specimens in the form of sandwiched films approx. 0.5 mm thick were assembled with extrusion direction vertical. The (120) and (032) crystal planes of commonly found monoclinic form of PEO were analyzed (diffraction maxima centered around $2\theta = 19.2^{o}$ and 23.3^{o}, respectively) and the respective pole figures were constructed. Experimental diffraction data were corrected for background scattering, sample absorption and defocusing of the beam. All pole figures were plotted with the POD program (Los Alamos National Lab, NM). Other details of the experimental procedure were described elsewhere (S6).

Results and Discussion

DSC analysis. **Figure S2** shows the first melting thermograms of layered EAA/PEO films with total thickness of about 120 μm and 1025 alternating layers, together with EAA and PEO control films. The PEO control film exhibited a sharp melting endotherm with peak melting temperature T_m at 65 °C. The EAA control film exhibited a broad melting endotherm with the melting peak at 97 ºC. The crystallinity calculated from ΔH_m was 78 wt% for PEO and 34 wt% for EAA using the heat of fusion

(ΔH^o) values of 197 J g^{-1} for PEO crystals (S7) and 290 J g^{-1} for polyethylene crystals (S8). All the layered films exhibited a melting peak for the EAA constituent at 97 ºC in the heating thermograms, corresponding to the melting temperature that of the EAA control films. The peak melting temperature for the PEO constituent in the layered films was about 2~3^{o}C lower than that of the PEO control film. The measured values of $\Delta H_{m,total}$ of the layered films were close to the calculated additive value from film composition. Separation of the enthalpy contribution of the PEO layers ($\Delta H_{m,PEO}$) from the total melting enthalpy ($\Delta H_{m,total}$) was performed and the crystallinity of the PEO layers was calculated based on $\Delta H_{m,PEO}$ and the PEO content in the films (**Table S2**). The crystallinity of PEO in the layers was close to that of the PEO control film.

SAXS analysis. **Figure S3** shows the 2-dimensional SAXS patterns of EAA/PEO films with 3.6 μm, 110 nm and 20 nm PEO layers where the incident X-ray beam was parallel to the normal direction (ND) and to the extrusion direction (ED). Because the SAXS patterns measured in the transverse direction (TD) were indistinguishable from those in the ED, only ED and ND patterns are presented in the following discussion. The intense meridional streak in the ED patterns was mainly associated with grazing incidence scattering. This scattering was found to veil weak scattering from the lamellae. For clarification, the equatorial and meridional scattering profiles were extracted from the 2D patterns and are depicted in **Figure S4**. The peak assignments were based on the peak positions of the PEO and EAA control films in **Figure S4A**. Comparison of the various scattering profiles indicated that the first-order peak positions of the PEO and EAA lamellae in coextruded EAA/PEO films remained nearly the same as in the control films. The long periods, $L_p=2\pi/q$, for PEO and EAA

lamellae obtained from the SAXS measurements were 22.0 ± 0.6 nm and 10.8 ± 0.5 nm, respectively. The long period of PEO was consistent with literature reports for this molecular weight (S9).

The ND and ED profiles from 3.6 μm PEO layers (**Figure S4B**) showed almost the same peak sharpness and height as the PEO control films implying that the PEO layers were too thick for PEO lamellae to feel any significant confinement effect. The slight increase in the meridional intensity over the equatorial intensity in the ND patterns was attributed to the melt flow during coextrusion.

As the PEO layer thickness decreased to 110 nm and 20 nm (**Figure S4C** and **D**, respectively), highly oriented scattering features of the PEO lamellae appeared. These were due to the spatial confinement, not to a mechanical flow effect. The scattering peak of PEO lamellae in the ED meridional pattern was much stronger and sharper than in the ED equatorial pattern, where it was barely discernable. Also, no first-order peak maximum for the PEO lamellae was discerned in the ND patterns. These scattering features implied that large-scale, oriented structures with the main scattering vector normal to the layer formed in the PEO layers. This was evidence that PEO lamellae were oriented primarily parallel to the layer surface. Crystallization as in-plane lamellae was due to the narrow confinement in the EAA layer interstices. The well-oriented, in-plane lamellae were not detected when the X-ray beam was parallel to the ND since this direction was along the projection direction of the lamellar stacks. The in-plane lamellae were totally different from the individual lamellae of a shish-kebab or a spherulite, which have only one growth face. Rather, they were more like single crystals.

Scattering from the 20 nm PEO layers was only detected on the meridian with the X-ray beam parallel to the ED. This implied a single population of in-plane lamellae that had grown in the direction parallel to the PEO layers. It was also noted that the first order peak maxima in the SAXS pattern from 20 nm layers was much weaker than that from 110 nm layers. If the lamellae were uncorrelated within the PEO layers, they should not show a first-order peak maximum in the SAXS pattern, and rather, should exhibit only single lamellar scattering features. Thus, it was thought that the observed weak lamellar correlation peak from 20 nm PEO layers was associated with the thickness distribution of the layers which occasionally enabled formation of two single crystals in a single PEO layer.

In contrast to the high degree of lamellar orientation in the PEO layers, the broad EAA first order SAXS reflection appeared in the ED and TD patterns with only a slight meridional concentration, which was especially evident in the ND profiles. The slight residual orientation of the EAA lamellae was attributed to the melt flow during coextrusion.

WAXS Analysis. The 2-dimensional transmission WAXS patterns from EAA and PEO films confirmed that EAA had the orthorhombic crystal form of polyethylene, and PEO took the usual monoclinic crystal form. The WAXS patterns of EAA/PEO layered films are shown in **Figure S5**. Because the WAXS patterns measured in the TD were indistinguishable from those in the ED, only ED and ND patterns are presented here. The EAA (110) reflection (scattering angle $2\theta = 21.5^{\circ}$), and the PEO (120) reflection ($2\theta = 19.2^{\circ}$) and (032) reflection ($2\theta = 23.3^{\circ}$) appear in the WAXS patterns (S*10*). The EAA (200) reflection ($2\theta = 23.6^{\circ}$), which was seen in the EAA pattern, was

superimposed on the stronger PEO (032) reflection. The ND and ED patterns from the coextruded films with 3.6 μm-thick PEO layers exhibited almost isotropic rings for reflections from both the PEO and the EAA layers, **Figure S5A**.

The ED pattern from the film with 110 nm PEO layers (**Figure S5B)** revealed considerable orientation of the PEO. The PEO (120) reflections appeared as equatorial arcs and the PEO (032) reflections as arcs at approximately +65º and -65º with respect to the vertical direction. In addition, the ($\bar{2}24$) and (024) reflections appeared at +45º and -45º with respect to the vertical direction. Decreasing the PEO layer thickness to 20 nm sharpened the arcs in the ED pattern to spots, **Figure S5C**. The ED pattern resembled the PEO fiber pattern (S*11*) and indicated that the *c*-axis of the PEO crystals was oriented along the ND, i.e. vertical to the layer plane.

The ND patterns from the 110 nm and 20 nm PEO layers showed strong scattering at all angles, suggesting that the lamellae were essentially randomly oriented in the layer plane. In contrast to the high degree of orientation in the PEO layers, the EAA (110) reflection appeared as an almost isotropic ring in the ED patterns with only a slight equatorial concentration in the ND pattern due to slight orientation of the EAA chains in the extrusion direction. No other specific orientation of the EAA crystallographic planes was observed, although the EAA layers in these two samples were less than 400 nm thick. It was highly unlikely that the slight residual orientation of EAA from the extrusion process affected the oxygen permeability.

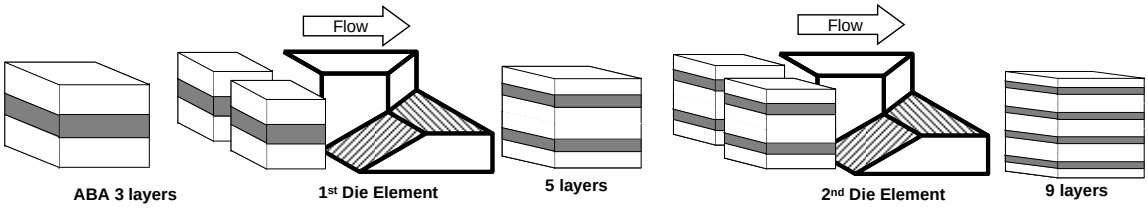

Figure S1. Layer-multiplying coextrusion for forced-assembly of polymer nanolayers. After the polymer melts are combined in the ABA feedblock, the melt stream flows through a series of layer-multiplying die elements; each element splits the melt vertically, spreads it horizontally, and finally recombines it with twice the number of layers. The figure illustrates how two elements multiply the number of layers from 3 to 9. An assembly of n die elements produces $2^{(n+1)}+1$ layers with polymer A layers on both sides of the film. Finally, the melt is spread in a film die to further reduce the layer thickness.

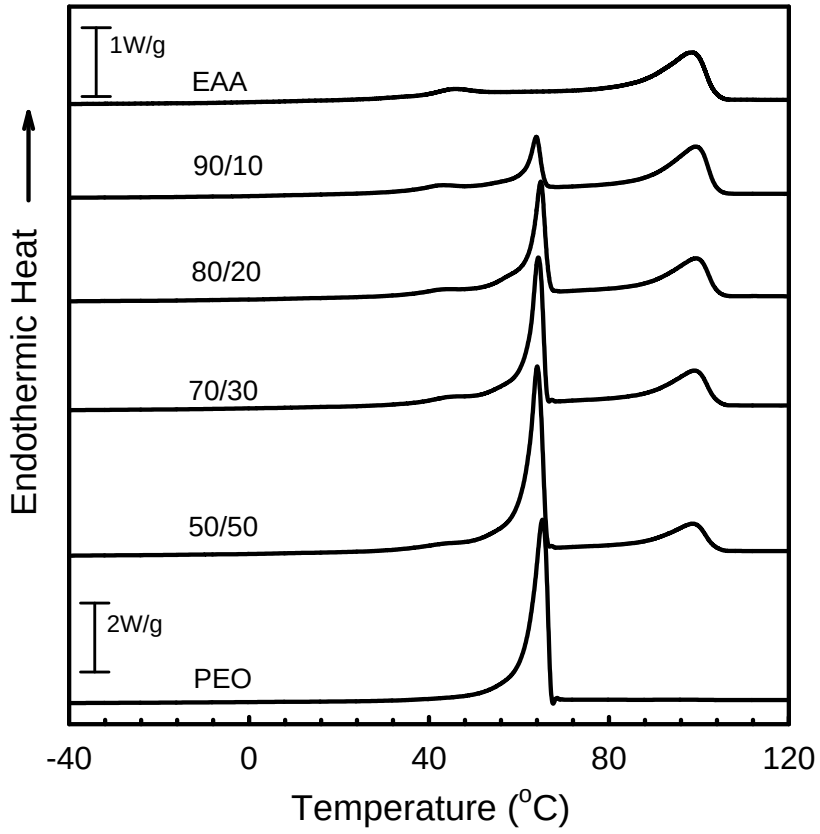

Figure S2 The first heating thermograms of EAA/PEO films with 1025 alternating layers and total thickness about 120μm. The EAA/PEO compositions (v/v) are as labeled. The heating rate was 10°C/min.

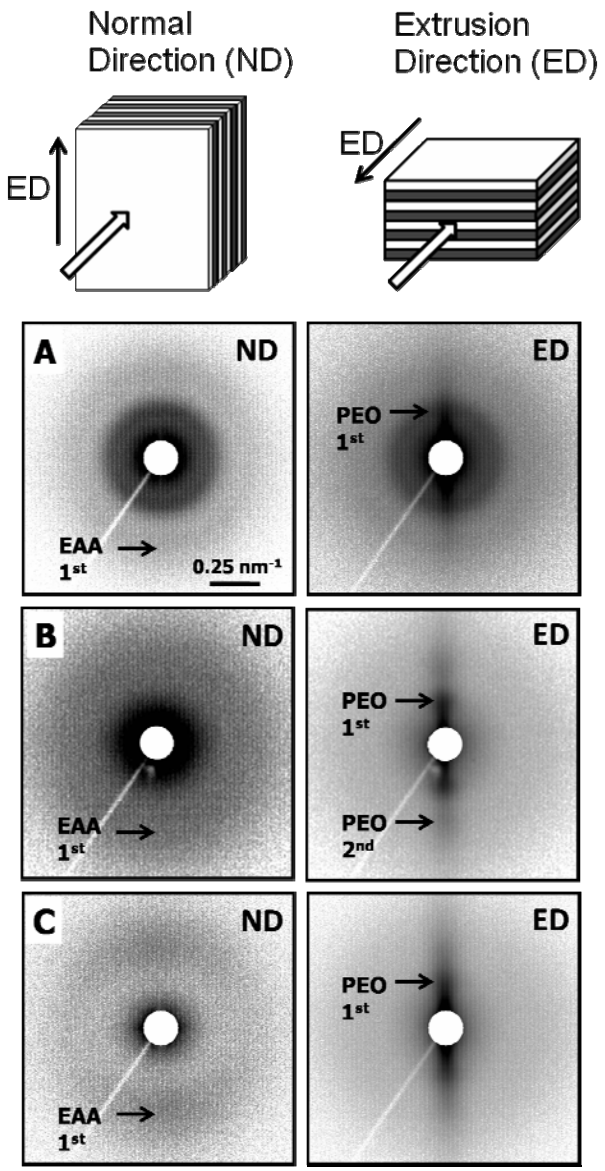

Figure S3 The 2D SAXS patterns of EAA/PEO films with different PEO layer thicknesses. The patterns were measured along the normal direction (ND) and the extrusion direction (ED): (A) 3.6 μm PEO layers; (B) 110 nm PEO layers; and (C) 20 nm PEO layers. The PEO first-order, PEO second-order and EAA first-order peaks are marked with arrows. The scale bar in (A) defines the scattering vector q scale. The intense meridional streak in the ED patterns is due to grazing incidence scattering.

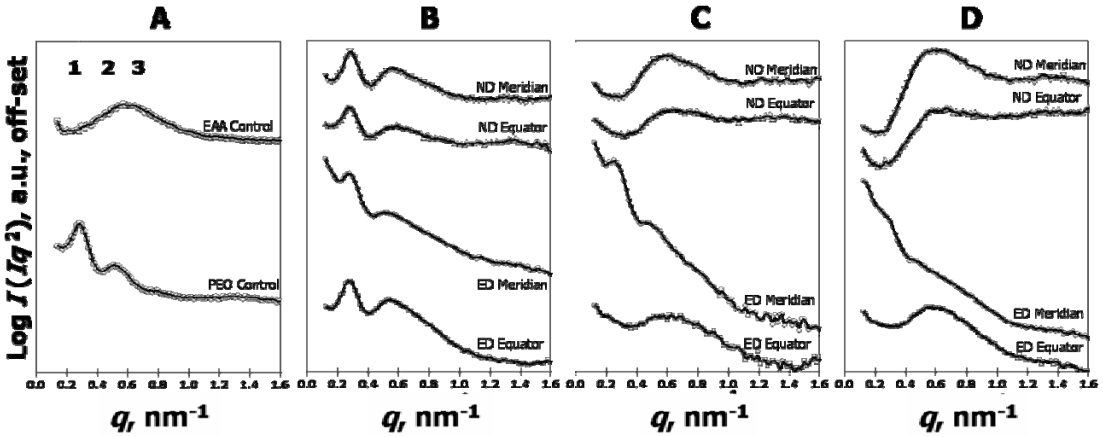

Figure S4 The 1D equatorial and meridional SAXS slices were extracted from the 2D images. (A) The control films showed the first and second order PEO small-angle reflections and the first order EAA reflection, which are indicated by the vertical lines. (B) The ND and ED profiles from the 3.6 μm PEO layers show almost the same peak sharpness and height as the PEO control indicating that the PEO layers are essentially isotropic and too thick for the lamellae to feel any significant confinement effect. (C) Strong small-angle scattering from 110nm PEO layers only in the ED meridional slice shows that the PEO lamellae are oriented primarily in the plane of the layer. (D) Weak small-angle PEO scattering from 20 nm layers in the ED meridional slice suggests primarily single, isolated lamellae.

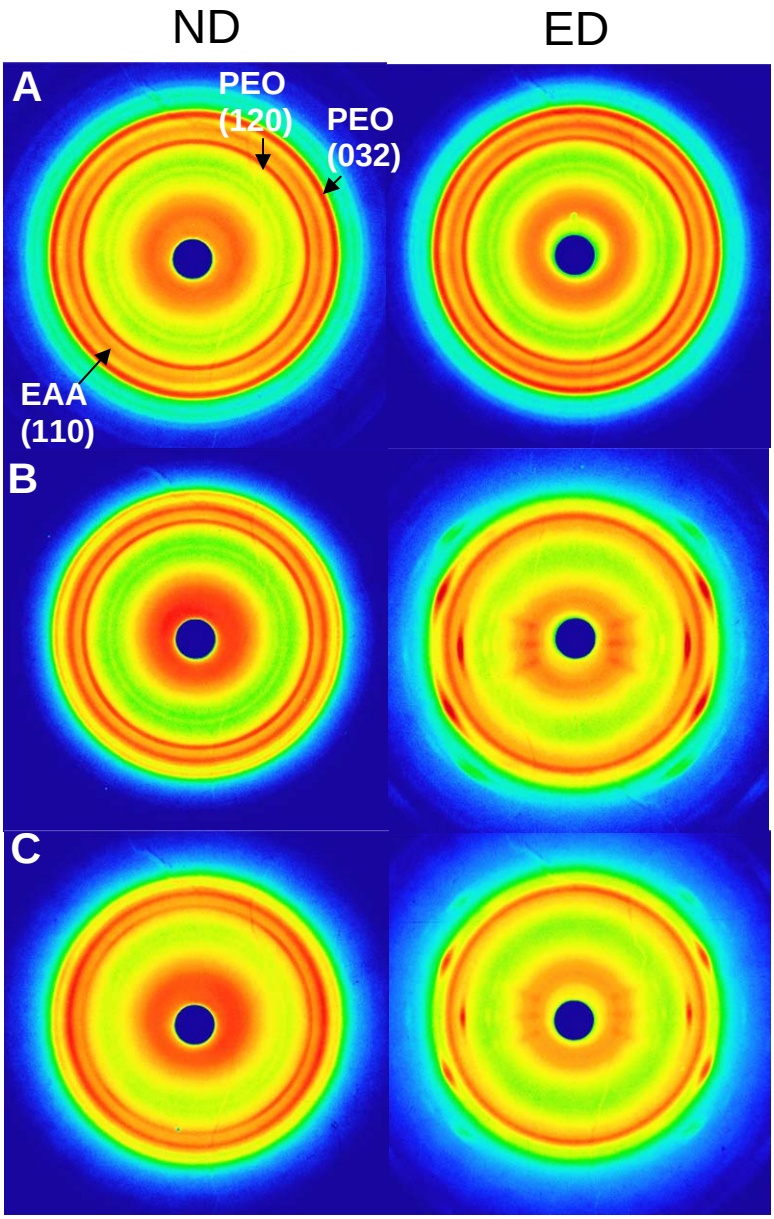

Figure S5 The 2D WAXS patterns of EAA/PEO films with different PEO layer thicknesses. (A) The ND and ED patterns from the 3.6 μm PEO layers confirm the usual monoclinic crystal form of PEO and show the isotropic orientation of the unit cell. (B) The ND and ED patterns from the 110 nm PEO layers show a high degree of orientation with the *c*-axis vertical to the layer plane. (C) Arcs in the WAXS ED pattern of 110 nm PEO layers are sharpened to spots in the WAXS ED pattern of 20 nm PEO layers.

Table S1 Film composition, number of layers, film thickness and nominal PEO layer thickness of EAA/PEO films

EAA/PEO (v/v)	Number of layers	Film Thickness (μm)	Nominal PEO layer Thickness (nm)
0/100	1025	110	--
50/50	33	115	3600
70/30	33	110	2060
50/50	257	282	1100
50/50	257	130	510
70/30	257	120	280
50/50	257	46	180
50/50	1025	127	125
70/30	1025	190	110
70/30	257	38	90
70/30	1025	119	70
80/20	1025	133	50
50/50	1025	47	45
70/30	1025	51	30
80/20	1025	61	25
90/10	1025	107	20
90/10	1025	42	8
100/0	1025	121	--

Table S2 Melting enthalpies of EAA/PEO films with 1025 alternating layers

EAA/PEO (v/v)	EAA/PEO (wt/wt)	Film Thickness (μm)	Nominal PEO Layer Thickness (nm)	$\Delta H_{m, EAA}$[a] (J/g)	$X_{c,EAA}$[b] (wt%)	$\Delta H_{m, PEO}$[c] (J/g)	$X_{c,PEO}$[d] (wt%)
100/0	100/0	121	--	98	34	--	--
90/10	87/13	107	20	98	34	138	70
80/20	75/25	133	50	96	33	156	79
70/30	64/36	119	70	102	35	150	76
50/50	43/57	127	125	102	35	144	73
0/100	0/100	110	--	--	--	153	78

[a] heat of melting normalized to the weight fraction of the EAA layers
[b] calculated crystallinity of the EAA layers
[c] heat of melting normalized to the weight fraction of the PEO layers
[d] calculated crystallinity of PEO the layers

References

S1 C. D. Mueller, S. Nazarenko, T. Ebeling, T. L. Schuman, A. Hiltner, E. Baer, *Polym. Eng. Sci.* **37**, 355-362 (1997).

S2 T. E. Bernal-Lara, A. Ranade, A. Hiltner, E. Baer, in *Mechanical Properties of Polymers Based on Nanostructure*, 1st edition, G. H. Micheler, F. Balta-Callaja, Eds. (CRC press, Boca Raton, Florida 2005), pp. 629-682.

S3 D. J. Sekelik, E. V. Stepanov, S. Nazarenko, D. Schiraldi, A. Hiltner, E. Baer, *J. Polym. Sci. Pt. B-Polym. Phys.* **37**, 847-857 (1999).

S4 H. Lin, B. D. Freeman, *J. Membrane Sci.* **239**, 105 (2004).

S5 L. E. Alexander, *X-Ray Difraction Methods in Polymer Science* (Wiley: New York, 1969).

S6 M. Pluta, Z. Bartczak, A. Galeski, *Polymer* **41**, 2271-2288 (2000)

S7 C. Campbell, K. Viras, M. J. Richardson, A. J. Masters, C. Booth, *Makromol. Chem.* 1993, 194, 799.

S8 Wunderlich, B. Macromolecular Physics, Vol. 3; Academic Press: New York, 1980, 42.

S9 L. Zhao, W. Kai, Y. He, B. Zhu, Y. Inoue *J. Polym. Sci. Part B: Polym. Phys.* **43**, 2665-2676 (2005)

S10 The PEO reflection labeled (032) actually contains overlapped reflections from (032), ($\bar{1}$32), (112), ($\bar{2}$12), ($\bar{1}$24), ($\bar{2}$04) and (004) which have similar *d*-spacing of ~0.39nm with that from (032) being the strongest. They cannot be easily separated in (032) pole figure. Details can be found in L. Zhu et al, *J. Am. Chem. Soc.* **122**, 5957-5967 (2000).

S11 Y. Takahashi, H. Tadokoro, *Macromolecules* **6**, 672-675 (1973).